Computer Modeling of Crystalline Electrolytes: Lithium Thiophosphates and Phosphates

N. D. Lepley and N. A. W. Holzwarth [*,z]

Department of Physics, Wake Forest University, Winston-Salem, North Carolina 27109, USA

First principles modeling techniques are used to examine the stabilities, structures, and Li ion migration properties of (thio)phosphate electrolyte materials focusing on the "superionic" electrolyte $Li_7P_3S_{11}$. Our simulations find a stable structure for $Li_7P_3S_{11}$ that is in approximate agreement with X-ray and neutron diffraction experiments. The calculated formation energy predicts the structure to be unstable with respect to decomposition into Li_3PS_4 and $Li_4P_2S_6$ plus excess S which has been observed experimentally under certain preparation conditions. The minimum activation energy for Li ion migration is estimated to $E_A = 0.15$ eV for a vacancy mechanism, a result which approximates the value of $E_A = 0.12$ eV determined from temperature-dependent conductivity measurements. Within the accuracy of the calculations, some vacancy-interstitial pair formation energies are found to be $E_f \approx 0$. These low energy vacancy-interstitial pair formation processes contribute to the "superionic" properties of this material. For comparison, simulations on hypothetical phosphate and phosphonitride materials with similar crystal structures are presented and the results are analyzed in terms of possible connections to LiPON electrolytes.
© 2012 The Electrochemical Society. [DOI: 10.1149/2.jes113225] All rights reserved.

During the last 5 years, lithium thiophosphate solid electrolyte materials have been developed[1–7] for use in all-solid-state rechargeable batteries. In particular, crystalline $Li_7P_3S_{11}$ has been characterized as a superionic conducting material[3–6] possessing room temperature conductivities as high as 10^{-3} S/cm, which is 1000 times greater than that of the commercial solid electrolyte material LiPON.[8] Building on our previous work,[9] we report on computer modeling studies of this material as well as those of related phosphates and nitrided phosphates. The study includes both materials directly related to experimental observations as well as materials based on hypothetical structures. We present results on metastable crystal structures, formation energies, and mechanisms of Li ion migration.

We first summarize the so-called "first-principles" computational methods used in this study. Computed heats of formation and structural forms of several (thio)phosphate and related materials, are presented and and the relative stabilities of the materials are examined. Li ion conductivity in $Li_7P_3S_{11}$ and related materials is estimated in terms of energy barriers for Li ion vacancy and interstitial migration.

Computational Methods

The calculational methods are based on density functional theory.[10,11] Results were obtained using ultra-soft pseudopotentials (USPP)[12] and the *pwscf*[13] code. The exchange-correlation functional was the local density approximation[14] (LDA). In order to quantify numerical errors due to pseudopotential generation, we also performed some of the calculations using the projector augmented wave (PAW)[15] formalism. The PAW basis and projector functions were generated by the *atompaw*[16] code and used in both the *abinit*[17] and *pwscf*[13] packages. The USPP and PAW results showed nearly identical results, with a maximum difference in heats of formation of 0.01 eV/atom as reported in the *Transactions* paper associated with this work.[18] Visualizations were constructed using the *OpenDX*[19] and *XCrySDEN*[20] software packages. Further details regarding the computational methods are described in our previous work.[9,21]

For analyzing formation energies and other perfect crystal properties, calculations were performed with plane wave expansions of the wavefunction including $|\mathbf{k} + \mathbf{G}|^2 \leq 64$ bohr^{-2} and relatively dense sampling of the Brillouin zone. For example, crystals of $Li_7P_3S_{11}$ were calculated with a Monkhorst-Pack[22] $\mathbf{k}$-point sampling of $3 \times 6 \times 3$. For analyzing Li ion migration in $Li_7P_3S_{11}$, $Li_7P_3O_{11}$, and $Li_8P_3O_{10}N$, a fixed volume supercell of $1 \times 2 \times 1$ units was constructed. This

choice of supercell has approximately equal cell lattice vectors and remains a computationally manageable size – 84–88 atoms. Since only relative energies are important for this part of the study, less stringent convergence parameters could be used – namely – $|\mathbf{k} + \mathbf{G}|^2 \leq 32$ bohr^{-2} and a single $\mathbf{k}$-point sampling of the Brillouin zone.

Estimates of the migration energies E_m for the Li ion diffusion were calculated using the nudged elastic band (NEB) method[23–25] as implemented in the *pwscf* code. For each migration path studied, the migration energy E_m is determined as the difference between the maximum and minimum supercell energies calculated along the migration path. Because each metastable defect configuration involves a certain amount of distortion for each type of atom in the "host" lattice, it is useful to have a quantitative measure of this distortion. We can define an average distortion parameter for each defect in the form

$$\mathcal{D}^{\text{Def}}_{\text{atom}} \equiv \frac{1}{N_{\text{atom}}} \sum_{a \in \text{atom}} \left| \mathbf{R}^a_{\text{Def}} - \mathbf{R}^a_{\text{Ref}} \right|. \quad [1]$$

For each atom a of the "host" lattice, the distortion measures the displacement of the relaxed defect coordinate $\mathbf{R}^a_{\text{Def}}$ relative to the position of the corresponding site in the perfect lattice $\mathbf{R}^a_{\text{Ref}}$. N_{atom} denotes the number of atoms of a given atomic number in the simulation cell. In general, the distortion of one or two sites in the local neighborhood of the defect is substantially higher than the mean, so that another useful measure is the maximum distortion defined as

$$\mathcal{M}^{\text{Def}}_{\text{atom}} \equiv \max_{a \in \text{atom}} \left| \mathbf{R}^a_{\text{Def}} - \mathbf{R}^a_{\text{Ref}} \right|. \quad [2]$$

Structural Optimization and Heats of Formation

The results of density functional calculations include the ground state energy per unit cell, obtained with variational accuracy. Therefore, we expect the heats of formation of these materials to be well approximated. We have calculated the heats of formation for many of the Li (thio)phosphates and related materials as presented in Table I. The standard state reference energies were obtained in the same way as described in our earlier work (Ref. 9 and 21). The present results obtained using the ultra-soft pseudopotential scheme (labeled "CALC") differ slightly from the earlier work. This is due to more stringent convergence parameters and a slight readjustment of the standard energy of O on the basis of additional calorimetry data[26] for Li_2O_2, SO_3, and Li_2SO_4 using the structural determinations of references 28, 29, and 30, respectively. The comparison of all of the calculated results with experimental measurements show an average deviation of 0.2 eV/formula unit. The largest deviations are for $LiNO_3$ (0.5 eV/formula unit), Li_3PO_4 and Li_2S (0.3 eV/formula unit) and

* Electrochemical Society Active Member.
z E-mail: natalie@wfu.edu

Table I. Heats of formation ΔH (eV per formula unit) calculated for the lithium (thio)phosphate and related materials, comparing calculated results with experimental measurements[26] when available. Also listed are the structures assumed for the calculations, described in terms of the space group using the notation of Ref. [27].

Material	Structure	ΔH (eV per formula unit)	
		(CALC)	(EXP)
Li_2S	$Fm\bar{3}m$ (#225)	− 4.29	− 4.57
Li_2S_2	$P6_3/mmc$ (#194)	− 4.09	
γ-Li_3PS_4	$Pmn2_1$ (#31)	− 8.36	
β-Li_3PS_4	$Pnma$ (#62)	− 8.17	
$Li_4P_2S_6$	$P\bar{3}1m$ (#162)	− 12.41	
$Li_4P_2S_7$	$P\bar{1}$ (#2)	− 11.58	
$Li_7P_3S_{11}$	$P\bar{1}$ (#2)	− 20.00	
$Li_7P_3S_{11}^*$	$P\bar{1}$ (#2)	− 19.93	
Li_2O	$Fm\bar{3}m$ (#225)	− 6.18	− 6.20
Li_2O_2	$P6_3/mmc$ (#194)	− 6.54	− 6.57
β-Li_3PO_4	$Pmn2_1$ (#31)	− 21.41	
γ-Li_3PO_4	$Pnma$ (#62)	− 21.38	− 21.72
$Li_4P_2O_6$	$P\bar{3}1m$ (#162)	− 30.03	
$Li_4P_2O_7$	$P\bar{1}$ (#2)	− 34.26	
$Li_7P_3O_{11}$	$P\bar{1}$ (#2)	− 55.32	
α-Li_3N	$P6/mmm$ (#191)	− 1.64	− 1.71
γ-Li_3N	$Fm\bar{3}m$ (#225)	− 1.19	
$Li_5P_2O_6N$	$P\bar{1}$ (#2)	− 33.49	
$Li_8P_3O_{10}N$	$P\bar{1}$ (#2)	− 54.85	
SO_3	$Pna2_1$ (#33)	− 4.83	− 4.71
Li_2SO_4	$P2_1/a$ (#14)	− 14.73	− 14.89
$LiNO_3$	$R\bar{3}c$ (# 167)	− 5.49	− 5.01
h-P_2O_5	$R3c$ (#161)	− 15.54	− 15.53
α-P_3N_5	$C2/c$ (#15)	− 3.24	− 3.32

Li_2SO_4 (0.2 eV/formula unit). The remaining 6 formation energies for which comparison is possible deviate by 0.1 eV/formula unit or less.

A recent experimental study[31] of crystal phase transitions in Li_3PS_4 is consistent with our calculated formation energies of this material. The experimental group[31] found the low temperature stable structure to have the space group $Pmn2_1$ which they labeled γ-Li_3PS_4. This material has the same symmetry as β-Li_3PO_4. The experimental group determined the high temperature stable structure to have the space group $Pmna$ which they labeled β-Li_3PS_4. This structure which was also reported by earlier experiments,[32] has fractional occupancy of some of the Li sites, but is otherwise similar to the structure of γ-Li_3PO_4. Consistent with the experimental findings, our calculations find the so-called γ-Li_3PS_4 structure to have a formation energy 0.1 eV lower than all the modifications of the β-Li_3PS_4 structure that we studied.

The focus of the present work is on materials related to the superionic conductor $Li_7P_3S_{11}$. Starting with initial coordinates reported from experimental measurements[3,7] and maintaining the $P\bar{1}$ symmetry, the most stable structure was found with a formation energy of −20.00 eV/formula unit and another metastable structure was found (which we label $Li_7P_3S_{11}^*$) with a formation energy that is higher by 0.07 eV. Interestingly, the lowest energy structure was found by optimizing the reported coordinates derived from X-ray scattering analysis[3] while the metastable structure was found by optimizing the reported coordinates derived from neutron scattering results.[7] We were unable to find a transformation mechanism between the two structures, and results for both structures are presented. The fact that there are two (meta)-stable structures of crystalline $Li_7P_3S_{11}$ (and perhaps others as well), is not inconsistent with experimental investigations of various preparation methods.[5,6] Recent experiments[5] conclude that $Li_7P_3S_{11}$

Table II. Decomposition energies (in eV per formula unit) calculated from heats of formation results. Positive energies indicate that starting material is stable with respect to indicated reaction.

Reaction	ΔH (eV)
$Li_7P_3S_{11} \rightarrow Li_3PS_4 + Li_4P_2S_7$	0.06
$Li_7P_3S_{11}^* \rightarrow Li_3PS_4 + Li_4P_2S_7$	−0.01
$Li_7P_3S_{11} \rightarrow Li_3PS_4 + Li_4P_2S_6 + S$	−0.78
$Li_7P_3S_{11}^* \rightarrow Li_3PS_4 + Li_4P_2S_6 + S$	−0.85
$Li_7P_3O_{11} \rightarrow Li_3PO_4 + Li_4P_2O_7$	−0.35
$Li_8P_3O_{10}N \rightarrow Li_3PO_4 + Li_5P_2O_6N$	−0.06

is a high temperature crystalline phase which can be quenched to room temperature. The fact that the experimental reports indicate sensitivity to processing conditions seems consistent that multiple (meta)-stable crystalline structures can exist.

From the formation energy analysis, we are able to develop a rough idea about the stability of $Li_7P_3S_{11}$ and $Li_7P_3S_{11}^*$ and the phosphate analogs. Table II lists calculated decomposition energies. Since our calculational error is relatively large, we cannot claim that our results are definitive. We do find that $Li_7P_3S_{11}$ in its lowest energy structure is expected to be stable with respect to decomposition into Li_3PS_4 (assumed to be in the low energy γ-Li_3PS_4 structure) and $Li_4P_2S_7$, while $Li_7P_3S_{11}^*$ is slightly unstable. However, crystalline $Li_4P_2S_7$ has not been identified in experiment and our simulations find it to be unstable relative to decomposition into $Li_4P_2S_6$ and excess S. Consequently, $Li_7P_3S_{11}$ and $Li_7P_3S_{11}^*$ are unstable with respect to the formation of $Li_4P_2S_6$ as well. In fact, the precipitation of $Li_4P_2S_6$ and Li_3PS_4 under some conditions in the preparation of $Li_7P_3S_{11}$ has been reported.[5,6] The fact that good quality crystalline $Li_7P_3S_{11}$ can be prepared at room temperature by quenching from high temperature suggests that there exists a significant kinetic barrier which prevents phase change to the equilibrium room temperature structure.

In addition to these thiophosphate materials, we were able to find metastable structures having the same symmetry for $Li_7P_3O_{11}$ and $Li_8P_3O_{10}N$. While to the best of our knowledge, neither of these crystals has been identified by experiment, studying them can provide insight into LiPON electrolytes[8] which have similar stoichiometries and perhaps similar local configurations. Our results predict $Li_7P_3O_{11}$ to be unstable with respect to decomposition into into Li_3PO_4 and $Li_4P_2O_7$, while the nitrided material $Li_8P_3O_{10}N$ is correspondingly less unstable with respect to decomposition into Li_3PO_4 and $Li_5P_2O_6N$.

The structure of the calculated low energy form of $Li_7P_3S_{11}$ is visualized in Fig. 1.[33] Deviations from the structures reported on the basis of diffraction experiments Refs. 3 and 7 are not easily identified in this visualization. The optimized lattice parameters for $Li_7P_3S_{11}$ and related materials are listed in Table III. Compared with the experimental measurements, for the lowest energy structure of $Li_7P_3S_{11}$, the calculations underestimate the lattice constants along the **a** and **c** axes as expected for LDA calculations. On the other hand, the results overestimate the lattice constant along the **b** axis, in contradiction to the usual systematic LDA error. For the metastable $Li_7P_3S_{11}^*$ the calculation underestimates all three lattice constants compared with experiment as is more common in LDA calculations. For the experimental structures the lattice parameters given in Ref. 3 (based on X-ray diffraction) and Ref. 7 (based on both X-ray and neutron diffraction) differ from each other by less than 1%.

Although the two experimental measurements of the lattice parameters for $Li_7P_3S_{11}$ are quite similar, there are measurable differences in the reported fractional coordinates as shown in Table IV. The X-ray[3] and neutron[7] measurements differ primarily in determining the locations of sites Li(2) and Li(7), which vary by a fractional difference of 0.2 along the **b** axis corresponding to approximately 1 Å in distance. Table IV also lists the fractional coordinates of the two different calculated structures $Li_7P_3S_{11}$ and $Li_7P_3S_{11}^*$, which show measurable variations with each other and with experiment. The variations in the

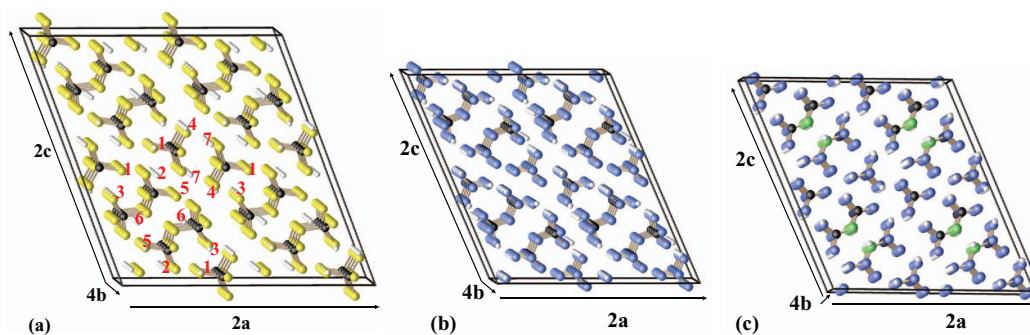**Figure 1.** (Color online.) Ball and stick diagrams of supercells of calculated optimized structures of (a): $Li_7P_3S_{11}$, (b): $Li_7P_3O_{11}$, and (c): $Li_8P_3O_{10}N$. Li, P, S, O, and N are indicated with white, black, yellow, blue, and green balls respectively. In (a) Li sites are indicated using the same numbering scheme as in Refs. 3 and 7, and the numbering for (b) and (c), while not shown, is analogous.

calculated atomic positions between the two structures and between the calculations and experiment average approximately 0.5 Å per atom, with the largest variations occurring in the Li positions. While structural differences between $Li_7P_3S_{11}$ and $Li_7P_3S_{11}^*$ are measurable, visualization in a plot from the perspective shown in Fig. 1 is quite subtle, which can be seen in Figs 4 and 6. These figures will be further discussed in connection with metastable interstitial sites. As we observe in our study of migrations and defect sites, even such subtle structural differences can have qualitative effects on Li ion behaviors.

As in our formation energy analysis, it is interesting to consider $Li_7P_3S_{11}$ in terms of Li_3PS_4 monomer and $Li_4P_2S_7$ dimer components. From this perspective one expects three Li sites to be associated with the monomer and four Li sites to be associated with the dimer. Examining the ball and stick diagram of $Li_7P_3S_{11}$ shown in Fig. 1, it appears that the monomer Li sites are **1**, **2**, and **7**, while the dimer Li sites are **2**, **3**, **5**, and **6**. However, analyzing the nearest $Li-^+$ distances, in the calculated structures we find that many of the Li^+ ions are virtually equidistant to sulfurs in both P_2S_7 and PS_4 groups. The details of Li ion placement differ slightly for the two calculated and two experimental structures. For the experimental structures, with a few exceptions, most of the distinct Li sites have nearest neighbor $Li-S$ separations which are at least 0.1 Å smaller than that of the next nearest neighbor. This contrasts with the calculated structures which show essentially equal $Li-S$ separations for the first two or three nearest neighbors.

In addition to data for $Li_7P_3S_{11}$, the lattice constants of the hypothetical $Li_7P_3O_{11}$ and $Li_8P_3O_{10}N$ materials are also shown in Table III. Not surprisingly, these crystals have smaller dimensions and somewhat different proportions than their thiophosphate analogs. These structures are also visualized in Fig. 1. While converging the optimal structure for $Li_7P_3O_{11}$, we found many metastable forms as might be expected for a naturally glassy material. The optimization of the $Li_8P_3O_{10}N$ structure was computationally more robust. Table V shows

Table III. Lattice parameters calculated for stable and metastable structures of $Li_7P_3S_{11}$, compared with experimental results (in parentheses). Lattice parameters calculated for metastable structures of $Li_7P_3O_{11}$ and $Li_8P_3O_{10}N$ are also listed.

	a (Å)	b (Å)	c (Å)	α (°)	β (°)	γ (°)
$Li_7P_3S_{11}$	12.00	6.16	12.25	102.5	113.8	72.1
$Li_7P_3S_{11}^*$	12.38	5.93	12.13	104.7	112.8	74.3
$Li_7P_3S_{11}$[a]	(12.50)	(6.03)	(12.53)	(102.8)	(113.2)	(74.5)
$Li_7P_3S_{11}$[b]	(12.48)	(6.03)	(12.50)	(102.9)	(113.3)	(74.5)
$Li_7P_3O_{11}$	9.58	4.99	10.46	103.0	116.4	72.4
$Li_8P_3O_{10}N$	9.62	4.85	10.46	103.1	115.8	75.3

[a] Ref. 4.
[b] Ref. 8.

Table IV. Fractional coordinates (x, y, z) of unique atomic sites in $Li_7P_3S_{11}$ ($P\bar{1}$ structure).

Site	Simulations	Experiments
Li(1)	$(0.669, 0.070, 0.094)$[a]	$(0.669, 0.132, 0.092)$[c]
	$(0.669, 0.065, 0.099)$[b]	$(0.676, 0.131, 0.145)$[d]
Li(2)	$(0.600, 0.549, 0.880)$[a]	$(0.638, 0.402, 0.866)$[c]
	$(0.632, 0.553, 0.885)$[b]	$(0.618, 0.623, 0.869)$[d]
Li(3)	$(0.199, 0.489, 0.707)$[a]	$(0.216, 0.530, 0.740)$[c]
	$(0.172, 0.526, 0.706)$[b]	$(0.268, 0.491, 0.735)$[d]
Li(4)	$(-0.030, 0.837, 0.251)$[a]	$(-0.058, 0.786, 0.270)$[c]
	$(-0.020, 0.801, 0.225)$[b]	$(-0.073, 0.832, 0.234)$[d]
Li(5)	$(0.299, 0.771, 0.298)$[a]	$(0.359, 0.591, 0.337)$[c]
	$(0.315, 0.792, 0.325)$[b]	$(0.315, 0.649, 0.282)$[d]
Li(6)	$(0.680, 0.648, 0.508)$[a]	$(0.637, 0.734, 0.498)$[c]
	$(0.669, 0.599, 0.488)$[b]	$(0.664, 0.751, 0.512)$[d]
Li(7)	$(0.129, 0.268, 0.116)$[a]	$(0.139, 0.294, 0.134)$[c]
	$(0.144, 0.114, 0.153)$[b]	$(0.122, 0.101, 0.129)$[d]
P(1)	$(0.780, 0.054, 0.452)$[a]	$(0.794, 0.033, 0.465)$[c]
	$(0.790, 0.030, 0.452)$[b]	$(0.792, 0.055, 0.473)$[d]
P(2)	$(0.472, -0.007, 0.273)$[a]	$(0.493, 0.038, 0.297)$[c]
	$(0.479, 0.002, 0.277)$[b]	$(0.489, 0.010, 0.300)$[d]
P(3)	$(0.830, 0.318, 0.057)$[a]	$(0.840, 0.270, 0.059)$[c]
	$(0.836, 0.275, 0.049)$[b]	$(0.843, 0.257, 0.071)$[d]
S(1)	$(0.822, 0.289, 0.598)$[a]	$(0.861, 0.236, 0.620)$[c]
	$(0.833, 0.280, 0.604)$[b]	$(0.852, 0.210, 0.640)$[d]
S(2)	$(0.811, 0.118, 0.314)$[a]	$(0.824, 0.105, 0.334)$[c]
	$(0.823, 0.070, 0.310)$[b]	$(0.832, 0.140, 0.353)$[d]
S(3)	$(0.853, -0.271, 0.488)$[a]	$(0.840, -0.317, 0.468)$[c]
	$(0.844, -0.299, 0.489)$[b]	$(0.840, -0.305, 0.465)$[d]
S(4)	$(0.583, 0.170, 0.425)$[a]	$(0.618, 0.160, 0.453)$[c]
	$(0.604, 0.171, 0.432)$[b]	$(0.609, 0.171, 0.444)$[d]
S(5)	$(0.304, 0.152, 0.294)$[a]	$(0.331, 0.227, 0.288)$[c]
	$(0.329, 0.197, 0.311)$[b]	$(0.323, 0.210, 0.283)$[d]
S(6)	$(0.478, 0.047, 0.120)$[a]	$(0.509, 0.080, 0.151)$[c]
	$(0.484, 0.052, 0.121)$[b]	$(0.524, 0.012, 0.158)$[d]
S(7)	$(0.521, -0.343, 0.302)$[a]	$(0.509, -0.300, 0.307)$[c]
	$(0.510, -0.344, 0.292)$[b]	$(0.513, -0.337, 0.302)$[d]
S(8)	$(0.820, 0.394, -0.102)$[a]	$(0.841, 0.330, -0.097$[c]
	$(0.832, 0.328, -0.113)$[b]	$(0.847, 0.329, -0.077)$[d]
S(9)	$(0.865, -0.028, 0.057)$[a]	$(0.828, -0.073, 0.046)$[c]
	$(0.844, -0.080, 0.036)$[b]	$(0.827, -0.091, 0.038)$[d]
S(10)	$(0.663, 0.474, 0.081)$[a]	$(0.678, 0.487, 0.064)$[c]
	$(0.685, 0.469, 0.084)$[b]	$(0.676, 0.480, 0.061)$[d]
S(11)	$(0.968, 0.429, 0.203)$[a]	$(0.977, 0.351, 0.188)$[c]
	$(0.977, 0.376, 0.196)$[b]	$(0.965, 0.376, 0.210)$[d]

[a] $Li_7P_3S_{11}$ simulation.
[b] $Li_7P_3S_{11}^*$ simulation.
[c] Ref. 4 (X-ray).
[d] Ref. 8 (Neutron).

Table V. Fractional coordinates (x, y, z) of unique atomic sites calculated for $Li_7P_3O_{11}$ and $Li_8P_3O_{10}N$ ($P\bar{1}$ structure).

Site	$Li_7P_3O_{11}$	$Li_7P_3O_{10}N$
Li(1)	(0.647, −0.106, 0.059)	(0.644, −0.099, 0.073)
Li(2)	(0.485, 0.534, 0.874)	(0.507, 0.505, 0.882)
Li(3)	(0.087, 0.601, 0.617)	(0.169, 0.553, 0.630)
Li(4)	(−0.055, 0.838, 0.260)	(−0.050, 0.861, 0.292)
Li(5)	(0.268, 0.666, 0.241)	(0.236, 0.688, 0.210)
Li(6)	(0.825, 0.609, 0.644)	(0.840, 0.606, 0.659)
Li(7)	(0.113, 0.278, 0.054)	(0.109, 0.267, 0.031)
Li(8)		(0.458, 0.348, 0.565)
P(1)	(0.784, 0.032, 0.473)	(0.734, 0.055, 0.476)
P(2)	(0.455, 0.050, 0.254)	(0.436, 0.092, 0.253)
P(3)	(0.831, 0.316, 0.082)	(0.834, 0.319, 0.107)
O(1)	(0.831, 0.212, 0.619)	(0.822, 0.200, 0.631)
O(2)	(0.836, 0.096, 0.368)	(0.823, 0.080, 0.385)
O(3)	(0.842, −0.284, 0.493)	(0.747, −0.268, 0.480)
O(4)/N	(0.591, 0.120, 0.409)	(0.555, 0.214, 0.412)
O(5)	(0.299, 0.262, 0.249)	(0.270, 0.272, 0.222)
O(6)	(0.503, 0.097, 0.141)	(0.487, 0.114, 0.134)
O(7)	(0.447, −0.252, 0.247)	(0.431, −0.227, 0.249)
O(8)	(0.879, 0.342, −0.037)	(0.891, 0.346, −0.005)
O(9)	(0.832, 0.005, 0.083)	(0.839, −0.001, 0.108)
O(10)	(0.663, 0.505, 0.062)	(0.665, 0.490, 0.075)
O(11)	(0.954, 0.427, 0.227)	(0.940, 0.449, 0.258)

the calculated fractional coordinates for $Li_7P_3O_{11}$ and $Li_8P_3O_{10}N$ for the lowest energy structures that we have found. Here we see that the additional Li (Li(8)) in the nitrided case relaxes to a position near the N that replaces the O at the bridge-bonding site.

Li Ion Migration Analysis

In order to study Li ion migration in these materials we have considered vacancy, interstitial, and composite mechanisms using the nudged elastic band (NEB) method[23–25] to estimate barriers for migration between metastable defect sites. While for such a complicated structure it is not possible to study all possible migrations, we considered several possibilities.

Analysis for $Li_7P_3S_{11}$ and $Li_7P_3S_{11}^*$—.Vacancy mechanism – $Li_7P_3S_{11}$.— The relaxed vacancy structures were determined by using a fixed volume $1 \times 2 \times 1$ supercell. In order to approximate the electrically insulating properties of the electrolyte, an extra electron was added to the system and compensated by a uniform positive charge. While no attempt was made to correct for supercell errors,[34] we expect relative configuration energies to be well-approximated. We first consider results determined for the most stable structure of $Li_7P_3S_{11}$, including vacancy defects at all 7 inequivalent Li sites.

For $Li_7P_3S_{11}$ the energies of the relaxed vacancy configurations relative to that of the most stable one (labeled **5**), as well as the distortion parameters defined in Eqs. 1 and 2 are given in Table VI. The low vacancy energies E_v indicate the sites where vacancy formation is energetically most favorable. In this case, the most favorable sites for vacancy formation are **5** and **6**, while the most energetically costly vacancy formation sites are **3** and **4**. The distortion parameters $\mathcal{D}_{atom}^{Vac}$ and $\mathcal{M}_{atom}^{Vac}$ are the greatest for the Li host atoms and the least for the P host atoms, while the S distortions are less than or similar to the Li distortions. The relatively small distortions of the S and P host atoms are presumably due to their covalent bonding within the monomer and dimer groups. Because the P atoms are anchored by several P−S bonds their distortions are further restricted.

In order to investigate a vacancy mechanism for Li ion migration, we performed NEB calculations for hopping between various vacancy sites. For each vacancy, NEB migrations to 5 or more nearest neighbors were computed. From these pairwise steps, sequential low

Table VI. Table of energies E_v (in eV) and distortions (in Å) for unique vacancy sites in $Li_7P_3S_{11}$ calculated for a $1 \times 2 \times 1$ supercell. The vacancy labels are given in Fig. 1 and the energies are given relative to the most stable site (5). The distortion parameters are calculated using Eqs. 1 and 2.

Label	E_v	$\mathcal{D}_{Li}^{Vac}/\mathcal{M}_{Li}^{Vac}$	$\mathcal{D}_{S}^{Vac}/\mathcal{M}_{S}^{Vac}$	$\mathcal{D}_{P}^{Vac}/\mathcal{M}_{P}^{Vac}$
1	0.23	0.11/0.53	0.10/0.52	0.05/0.10
2	0.11	0.14/0.46	0.10/0.46	0.06/0.12
3	0.27	0.11/0.44	0.08/0.31	0.04/0.08
4	0.28	0.07/0.26	0.05/0.23	0.03/0.04
5	0.00	0.09/0.31	0.06/0.26	0.04/0.09
6	0.07	0.09/0.73	0.05/0.15	0.04/0.07
7	0.24	0.09/0.26	0.07/0.24	0.05/0.12

energy hops were selected in order to estimate energy barriers E_m for migration along each crystallographic direction. These paths are shown in Fig. 2. While many of the hops between neighboring vacancy configurations have small energy barriers, E_m values for paths that traverse the supercell are determined by the maximum barriers along each path which are determined to be 0.43 eV, 0.29 eV, and 0.15 eV for the **c**, **a**, and **b** axes respectively. There are some common hops among some of the paths. However, the **1** ↔ **2** hops along the **a** and **c** axes are different, connecting equivalent sites in two distinct ways. Interestingly, there is significant structure in the energy diagrams between most of the metastable states, which is often associated with metastable interstitial positions occupied by host atoms during the vacancy migration step. The lowest migration barrier that we found for this material is 0.15 eV for net migration along the **b** axis involving zig-zag hops between the **4** ↔ **3** sites. Assuming that the formation energy for vacancy-interstitial pairs is negligible (a fact consistent with our simulations) an activation energy of $E_m = 0.15$ eV for this material is close to the value of 0.12 eV measured in experiment.[2,4]

*Vacancy mechanism – $Li_7P_3S_{11}^*$.—*For comparison, it is interesting to study vacancies in the metastable structure $Li_7P_3S_{11}^*$. The list of vacancy energies is given in Table VII. While site **5** remains the most stable vacancy site, the energetic variation among the other vacancy sites is substantially different in this structure. A large part of this energetic variation is related to the instability of several vacancy sites in this structure, as indicated by the large values of $\mathcal{M}_{Li}^{Vac}$ for sites **3** and **4**. A more detailed analysis of the relaxed structure for a vacancy at site **4** shows that the Li from the neighboring host lattice site **7** is distorted to toward the vacancy by 2 Å (60% of the distance between the corresponding sites in the perfect lattice). This relaxation contributes substantially to $E_v(4)$ as evidenced by the energy found from a constrained relaxation of this site. We found the constrained relaxation energy of the **4** to be 0.27 eV, comparable to the full

Table VII. Table of energies E_v (in eV) and distortions (in Å) for unique vacancy sites in $Li_7P_3S_{11}^*$ calculated for a $1 \times 2 \times 1$ supercell. The vacancy labels are given in Fig. 1 and the energies are given relative to the most stable site (5) for this structure. The distortion parameters, calculated using Eqs. 1 and 2 can be compared with the analogous values in Table VI for the more stable $Li_7P_3S_{11}$ structure.

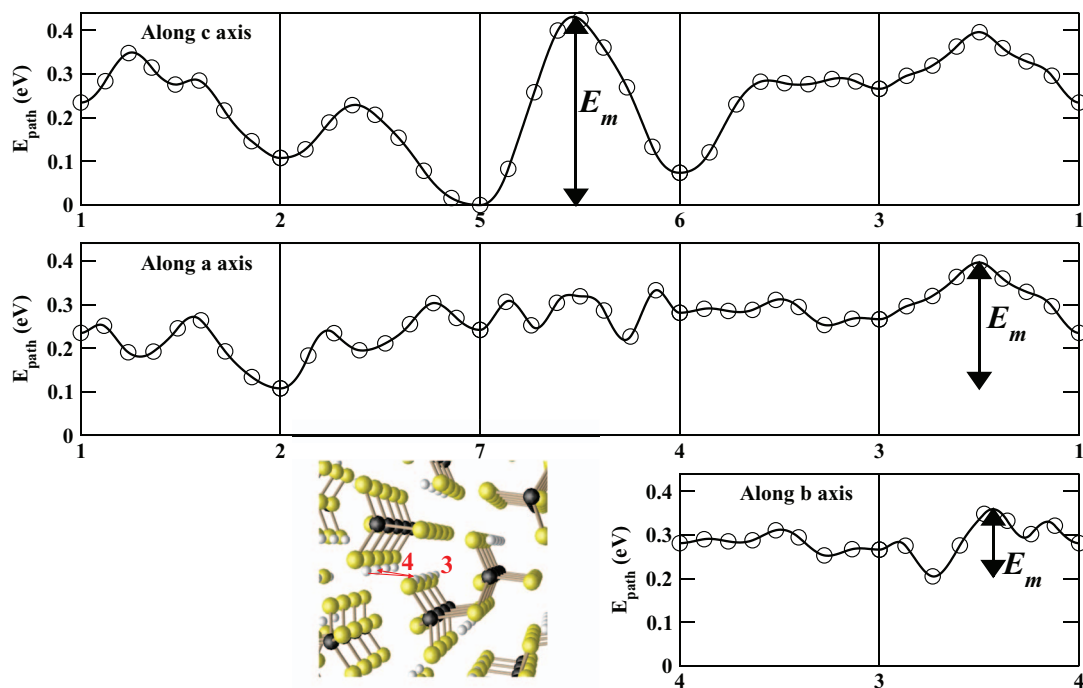| Label	E_v	$\mathcal{D}_{Li}^{Vac}/\mathcal{M}_{Li}^{Vac}$	$\mathcal{D}_{S}^{Vac}/\mathcal{M}_{S}^{Vac}$	$\mathcal{D}_{P}^{Vac}/\mathcal{M}_{P}^{Vac}$
1	0.38	0.15/1.00	0.07/0.18	0.04/0.07
2	0.27	0.16/0.88	0.08/0.29	0.05/0.11
3	0.27	0.34/1.69	0.15/0.50	0.07/0.11
4	0.16	0.33/2.17	0.11/0.38	0.06/0.13
5	0.00	0.11/0.25	0.08/0.34	0.05/0.08
6	0.19	0.13/0.28	0.07/0.21	0.04/0.07
7	0.22	0.15/1.04	0.07/0.25	0.04/0.09

Figure 2. (Color online.) Energy path diagram for Li ion vacancy migration in $Li_7P_3S_{11}$ between vacancies sites with net migration along the **c**-axis, **a**-axis, and **b**-axis. The points represent the calculated NEB images and the curve is interpolated. The horizontal scale is determined by the distances between NEB images, scaled to a unit distance between metastable configurations. The site labels are defined in Fig. 1. The energy scale is referenced to the lowest energy vacancy site **5**. Colored inset represents a visualization of the path between the **4** and **3** sites having net migration along the **b**-axis based on the perfect crystal structure.

relaxation energies of the **2** and **3** sites of this structure. Likewise for a vacancy at site **3**, the neighboring host lattice sites **4** and **7** are both strongly affected. For these unstable vacancy sites, the vacancy site labels are ambiguous.

For the $Li_7P_3S_{11}^*$ structure we carried out an NEB analysis similar to that described for the $Li_7P_3S_{11}$ structure. Due to the instabilities of the **3** and **4** sites, complete through paths corresponding to those presented in Fig. 2 are not possible. Figure 3 shows an example of a partial path compared with the corresponding path of the stable $Li_7P_3S_{11}$ structure. In this case, the migration barrier for the $Li_7P_3S_{11}$ structure is $E_m = 0.43$ eV because of the the hop between sites **5** and **6**. For the $Li_7P_3S_{11}^*$ structure, the barrier for this path is slightly greater due to the higher relative energies of sites **1** and **2**. This figure illustrates that while some similarities exist, in general the Li ion migration properties are sensitive to the details of the structure of these materials.

Interstitial mechanism – $Li_7P_3S_{11}$.—In addition to vacancy defects, it is possible to find many metastable sites capable of accommodating an excess Li ion in the $Li_7P_3S_{11}$ structure. A systematic search for these metastable sites was performed using a regular grid of possible sites.
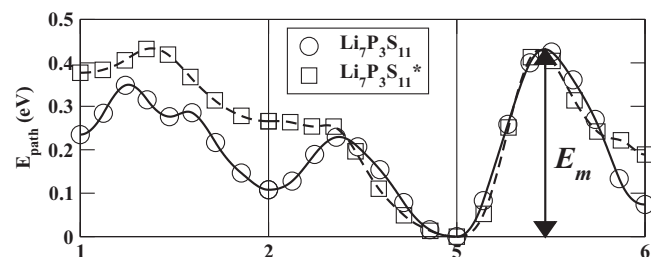
For each grid site, an interstitial Li ion was added to the perfect $1 \times 2 \times 1$ supercell and the system was allowed to relax at constant volume. As in the vacancy case, an electrically insulating system was approximated. An electron was removed from the system and compensated with a uniform negative charge. In order to best approximate the creation of a single interstitial defect, each interstitial site found from the grid search was added back to the perfect crystal and allowed to relax again. The low energy ($E_i < 0.2$ eV) relaxed interstitial positions found in this search are visualized in Fig. 4 superposed on the perfect lattice
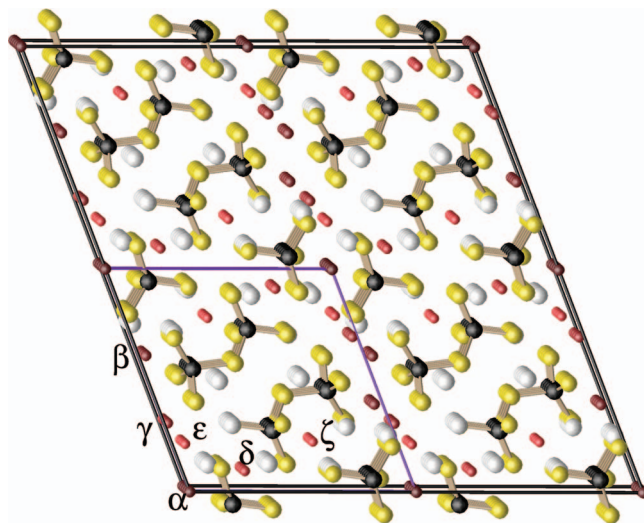

Figure 3. Energy path diagram for Li ion vacancy migration, comparing portions of the paths along the **c**-axis in in $Li_7P_3S_{11}$ and $Li_7P_3S_{11}^*$. The energy scale for each material is referenced to its lowest energy vacancy site (**5**).

Figure 4. (Color online.) Li ion interstitial sites visualized by superposition on the perfect $Li_7P_3S_{11}$ lattice. The interstitial sites are indicated with small dark red balls, using a dark to light variation to indicate the lowest to highest energy sites in the 0.00–0.19 eV energy scale. Inequivalent sites are labeled with Greek symbols.

Table VIII. Table of energies E_i (in eV) and distortions (in Å) for metastable interstitial sites in Li$_7$P$_3$S$_{11}$ calculated for a 1 × 2 × 1 supercell. The interstitial labels are given in Fig. 4 and the energies are given relative to the most stable site (α). The distortion parameters are calculated using Eqs. 1 and 2.

Label	E_i	$\mathcal{D}_{\mathrm{Li}}^{\mathrm{Int}}/\mathcal{M}_{\mathrm{Li}}^{\mathrm{Int}}$	$\mathcal{D}_{\mathrm{S}}^{\mathrm{Int}}/\mathcal{M}_{\mathrm{S}}^{\mathrm{Int}}$	$\mathcal{D}_{\mathrm{P}}^{\mathrm{Int}}/\mathcal{M}_{\mathrm{P}}^{\mathrm{Int}}$
α	0.00	0.24/1.60	0.08/0.23	0.05/0.08
β	0.07	0.13/0.99	0.08/0.28	0.06/0.11
γ	0.11	0.18/1.50	0.08/0.37	0.04/0.08
δ	0.11	0.48/1.83	0.18/0.49	0.10/0.18
ε	0.18	0.16/1.50	0.08/0.19	0.06/0.09
ζ	0.19	0.24/1.68	0.13/0.35	0.10/0.14

supercell. They represent 6 non-equivalent positions, the most stable of which (α) is located at the origin of our supercell. The energies E_i of these relaxed interstitial sites, relative to the α site, are listed in Table VIII along with the corresponding distortion parameters. Notably, we have found 6 distinct sites in an energy range of 0–0.2 eV, some of which are in close proximity to each other and to vacancy sites **3** and **4**. In addition to these reported low energy interstitial sites, some higher energy sites were also found. As an example, the energy of an interstitial defect at the inversion center is $E_i = 0.9$ eV, although other metastable interstitial defects in the vicinity of the inversion center were difficult to stabilize.

Since there are a number of interstitial sites in close proximity, it is possible to construct a migration path between them. The lowest energy path we found is along the **c**-axis and is presented in Figure 5. The migration barrier $E_m = 0.49$ eV is dominated by the hop between equivalent β sites. While the γ site is not explicitly labeled in this plot, it is represented by the local minimum in the energy path between the ε and β sites.

Interstitial mechanism – Li$_7$P$_3$S$_{11}^*$.—We have also examined the metastable interstitial sites in the Li$_7$P$_3$S$_{11}^*$ structure. Although the structural differences between the two structures is small, it is large enough to have an effect on the positions and relative energies of the metastable sites. Figure 6 shows the placement of the low energy metastable interstitial sites superposed on the perfect structure of the Li$_7$P$_3$S$_{11}^*$ crystal and Table IX shows the corresponding energies and host lattice distortions. Interestingly, the α, β, and ζ sites are metastable in both structures, while the Li$_7$P$_3$S$_{11}^*$ structure has two new sites we label η and θ, and the γ and δ sites from the Li$_7$P$_3$S$_{11}$ structure are not found. The site labeled η is close to the β site along the **a** and **c** axes but is shifted along the **b**-axis.

Combined vacancy-interstitial mechanism – Li$_7$P$_3$S$_{11}$.—In addition to the study of single defects in the 1 × 2 × 1 supercell, it is interesting to consider the formation of vacancy-interstitial pairs in Li$_7$P$_3$S$_{11}$. As shown in Table X, we found several examples of configurations with very low pair formation energies E_f and many of them have low activation barriers. In fact the energy of the **5ε** configuration has the unphysical value of $E_f < 0$. This is likely an artifact of the supercell due to dipolar images. The corresponding value in a 2 × 2 × 1 supercell is

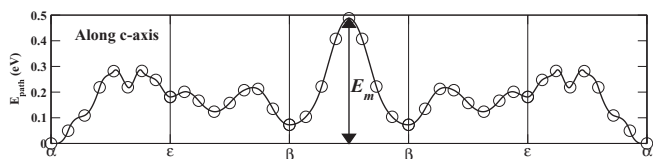**Figure 6.** (Color online.) Li ion interstitial sites visualized by superposition on the perfect Li$_7$P$_3$S$_{11}^*$ lattice. The interstitial sites are indicated with small dark red balls, using a dark to light variation to indicate the lowest to highest energy sites in the 0.00–0.26 eV energy scale. Inequivalent sites are labeled with Greek symbols.

less negative by 0.01 eV. Since the supercell image errors are sensitive to the geometries of the defects, we expect that the other values of E_f listed in Table X could also have errors in the neighborhood of ± 0.03 eV. Nevertheless the qualitative results of Table X indicate several examples of low energy vacancy-interstitial pair formations in Li$_7$P$_3$S$_{11}$.

The pair formation energy E_f relates to the experimentally measured temperature-dependent conductivity $\sigma(T)$ which follows an Arrhenius behavior of the form

$$\sigma(T) = \frac{\sigma_0}{T} e^{-E_A/kT}, \qquad [3]$$

where k denotes the Boltzmann constant, σ_0 denotes a temperature independent system constant, and the experimentally determined activation energy E_A is related to the calculated energies according to

$$E_A = E_m + E_f/2. \qquad [4]$$

For materials having small formation energies E_f such as Li$_7$P$_3$S$_{11}$, the measured activation energies E_A are dominated by the migration energies E_m.

In addition to considering vacancy-interstitial pair formation and single defect migration statistically independently, as indicated by the Arrhenius behavior 3, we have also investigated some possible concerted mechanisms involving both the vacancy and interstitial sites. One such example is given in Fig. 7 showing a process which starts with the perfect crystal followed by the formation of a

Figure 5. Energy path diagram for Li ion migration in Li$_7$P$_3$S$_{11}$ with a pure interstitial mechanism. The site labels are defined in Fig. 4 and the energy scale is referenced to the lowest energy site α.
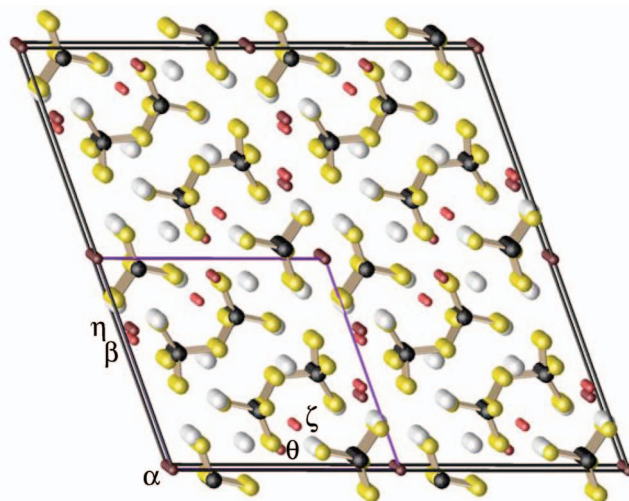
Table IX. Table of E_i energies (in eV) and distortions (in Å) for metastable interstitial sites in Li$_7$P$_3$S$_{11}^*$ calculated for a 1 × 2 × 1 supercell. The interstitial labels are given in Fig. 6 and the energies are given relative to the most stable site (α). The distortion parameters are calculated using Eqs. 1 and 2.

Label	E_i	$\mathcal{D}_{\mathrm{Li}}^{\mathrm{Int}}/\mathcal{M}_{\mathrm{Li}}^{\mathrm{Int}}$	$\mathcal{D}_{\mathrm{S}}^{\mathrm{Int}}/\mathcal{M}_{\mathrm{S}}^{\mathrm{Int}}$	$\mathcal{D}_{\mathrm{P}}^{\mathrm{Int}}/\mathcal{M}_{\mathrm{P}}^{\mathrm{Int}}$
α	0.00	0.14/0.33	0.07/0.22	0.03/0.04
β	0.14	0.15/1.38	0.08/0.26	0.06/0.10
ζ	0.26	0.21/1.14	0.08/0.21	0.04/0.09
η	0.10	0.38/1.96	0.11/0.30	0.08/0.11
θ	0.13	0.16/1.01	0.07/0.32	0.05/0.08

Table X. Table of vacancy-interstitial pair formation energies E_f (in eV) and the corresponding host lattice distortions (in Å) calculated using Eqs. 1 and 2. For several of the vacancy-interstitial pairs, a direct formation process can be identified. For those, the migration barriers E_m (in eV) and the separation R (in Å) of the vacancy and interstitial sites (estimated from the perfect lattice) are also reported.

Label	E_f	$\mathcal{D}_{Li}^{Pair}/\mathcal{M}_{Li}^{Pair}$	$\mathcal{D}_{S}^{Pair}/\mathcal{M}_{S}^{Pair}$	$\mathcal{D}_{P}^{Pair}/\mathcal{M}_{P}^{Pair}$	R	E_m
3β	0.05	0.06/0.17	0.05/0.18	0.03/0.06	1.93	0.09
5ε	−0.03	0.16/1.48	0.08/0.18	0.07/0.11	2.60	0.13
7ε	0.07	0.07/0.25	0.05/0.20	0.03/0.05	2.82	0.11
4γ	0.02	0.09/0.58	0.06/0.26	0.04/0.08	1.91	0.08
5α	0.01	0.28/1.66	0.10/0.24	0.05/0.09		
6α	0.10	0.35/1.69	0.11/0.29	0.09/0.14		
6β	0.14	0.15/1.11	0.12/0.31	0.10/0.15		

Table XI. Table of energies E_v (in eV) and distortions (in Å) for unique vacancy sites in $Li_7P_3O_{11}$ calculated for a $1 \times 2 \times 1$ supercell. The vacancy labels are given in Fig. 1 and the energies are given relative to the most stable site (4). The distortion parameters are calculated using Eqs. 1 and 2.

Label	E_v	$\mathcal{D}_{Li}^{Vac}/\mathcal{M}_{Li}^{Vac}$	$\mathcal{D}_{O}^{Vac}/\mathcal{M}_{O}^{Vac}$	$\mathcal{D}_{P}^{Vac}/\mathcal{M}_{P}^{Vac}$
1	0.12	0.06/0.22	0.05/0.18	0.04/0.07
2	0.02	0.16/2.45	0.09/0.31	0.06/0.12
3	0.01	0.06/0.30	0.06/0.29	0.04/0.09
4	0.00	0.09/0.97	0.06/0.34	0.04/0.07
5	0.39	0.05/0.12	0.06/0.31	0.04/0.11
6	0.26	0.05/0.19	0.04/0.19	0.03/0.07
7	0.12	0.05/0.15	0.05/0.27	0.03/0.07

vacancy-interstitial pair of type **4β**. In the simulation, it is assumed that the β interstitial site remains fixed while the vacancy continues to migrate along the **a**-axis. From this study, we see that at sufficient separation between the vacancy and interstitial defects their interaction effects are small so that the energy path diagram is very similar to that of the pure vacancy, which is superposed in the figure. For the path shown, the **4** vacancy migrates along the **a** and **b** axes to another **4** vacancy site which is no longer equivalent because it is further from the interstitial ion at the site β. The larger deviations of the energy path diagrams in the vicinity of the **7** site are due to a supercell image of the β interstitial in this calculation. The particular path shown in this diagram is unlikely to be important in Li ion migration. Not only does it have a large migration energy $E_m = 0.54$ eV, but the statistical probability of this concerted pair is much smaller than the probability of the single particle events.

Analysis for $Li_7P_3O_{11}$.— The metastable crystal $Li_7P_3O_{11}$ is structurally very similar to its thiophosphate analog and is visualized in Fig. 1. Using the same Li site labels given for the $Li_7P_3S_{11}$ structure, it is possible to analyze the Li ion migration in $Li_7P_3O_{11}$ in a similar way. The energies of the relaxed vacancy configurations relative to that of the most stable one (labeled **4**) and the corresponding distortion measures defined by Eqs. 1 and 2 for the 7 inequivalent Li ion vacancies are given in Table XI. In contrast to the thiophosphate material, the most favorable sites for vacancy formation in $Li_7P_3O_{11}$ are the **4** and **3** sites, while the least favorable are the **5** and **6** sites. Furthermore, the **2** vacancy site for this structure is unstable as indicated by its large value of $\mathcal{M}_{Li}^{Vac}$ due to the motion of the host lattice **3** site toward the vacancy.

As for the thiophosphate material, nearest neighbor NEB paths were computed and minimal energy through paths were constructed
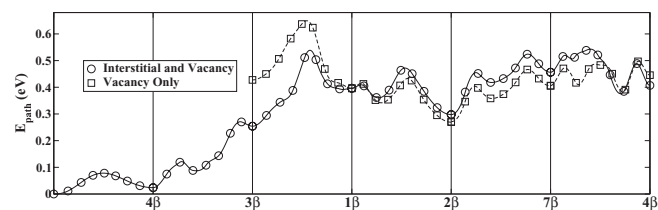
for $Li_7P_3O_{11}$. The energy path diagrams for net motion along the **a**, **b**, and **c** axes are presented in Fig. 8. Some of the steps involve symmetry equivalent sites such as **7 ↔ 7**. Along the **c** axis E_m is 0.54 eV and along the **a** axis E_m is 0.53 eV. For net migration along the **b**-axis, three of the paths have very similar values of E_m − 0.52, 0.52, 0.59 eV for the zig-zag hops between **4 ↔ 3**, **7 ↔ 7**, and **6 ↔ 5** sites, respectively. Figure 8 shows that the path corresponding to a Li ion migration migration energy of $E_m = 0.15$ eV in the $Li_7P_3S_{11}$ structure has a migration energy of $E_m = 0.52$ eV in $Li_7P_3O_{11}$ using the same supercell.

In order to estimate the results of supercell size, we performed very limited calculations for a $1 \times 4 \times 1$ supercell. The NEB path between sites **3** and **4** with net migration along the **b**-axis is shown in Fig. 9. While details of the path differ, the results are quite similar. The relative vacancy energies given in Table XI for the $1 \times 2 \times 1$ supercell differ by at most 0.03 eV from those calculated for the $1 \times 4 \times 1$ supercell.

In addition to studying the energies for Li ion migrations, we also studied the formation of vacancy-interstital pairs, estimating the lowest formation energy to be $E_f = 0.5$ eV with more typical formation energies in the neighborhood of $E_f = 0.8$ eV.

Analysis for $Li_8P_3O_{10}N$.— $Li_8P_3O_{10}N$ differs from the analogous $Li_7P_3O_{11}$ structure by the substitution of each bridge-bonding O with N and the addition of an extra Li near each N site as shown in Fig. 1. The energies of the relaxed vacancy configurations relative to that of the most stable one (labeled **3**), as well as the distortion parameters defined in Eqs. 1 and 2 are given in Table XII. In this case, because of a subtle accident of the geometry, the most stable vacancy site (**3**) is lower in energy by 0.3 eV than the other 7. The distortions induced by the vacancies are relatively small.

Figure 10 shows a possible Li ion vacancy migration path for this structure. While there may be paths with lower migration barriers,

Figure 7. Energy path diagram for Li ion migration in $Li_7P_3S_{11}$ with a both interstitial and vacancy involvement, starting with the perfect supercell followed by **4β** formation. In subsequent steps, the interstitial Li is held at the β site while the vacancy migrates along a path along the **a**-axis. The energy scale for this curve is referenced to the perfect crystal. In addition to the neutral pair migration, a portion of the pure vacancy path diagram is superposed on the figure (with energy shifted so that the two curves coincide at the **1** vacancy configuration).

Table XII. Table of energies E_v (in eV) and distortions (in Å) for unique vacancy sites in $Li_8P_3O_{10}N$ calculated for a $1 \times 2 \times 1$ supercell. The vacancy labels are given in Fig. 1 and Table V and the energies are given relative to the most stable site (3). The distortion parameters are calculated using Eqs. 1 and 2.

Label	E_v	$\mathcal{D}_{Li}^{Vac}/\mathcal{M}_{Li}^{Vac}$	$\mathcal{D}_{O}^{Vac}/\mathcal{M}_{O}^{Vac}$	$\mathcal{D}_{N}^{Vac}/\mathcal{M}_{N}^{Vac}$	$\mathcal{D}_{P}^{Vac}/\mathcal{M}_{P}^{Vac}$
1	0.33	0.05/0.16	0.04/0.25	0.03/0.08	0.03/0.07
2	0.27	0.07/0.62	0.05/0.24	0.03/0.04	0.03/0.08
3	0.00	0.05/0.41	0.04/0.30	0.02/0.03	0.02/0.06
4	0.36	0.08/0.89	0.06/0.23	0.05/0.10	0.03/0.06
5	0.31	0.05/0.13	0.05/0.26	0.03/0.03	0.03/0.07
6	0.39	0.04/0.20	0.04/0.26	0.03/0.04	0.03/0.08
7	0.35	0.04/0.14	0.05/0.24	0.03/0.08	0.03/0.06
8	0.37	0.05/0.28	0.04/0.25	0.08/0.14	0.03/0.07

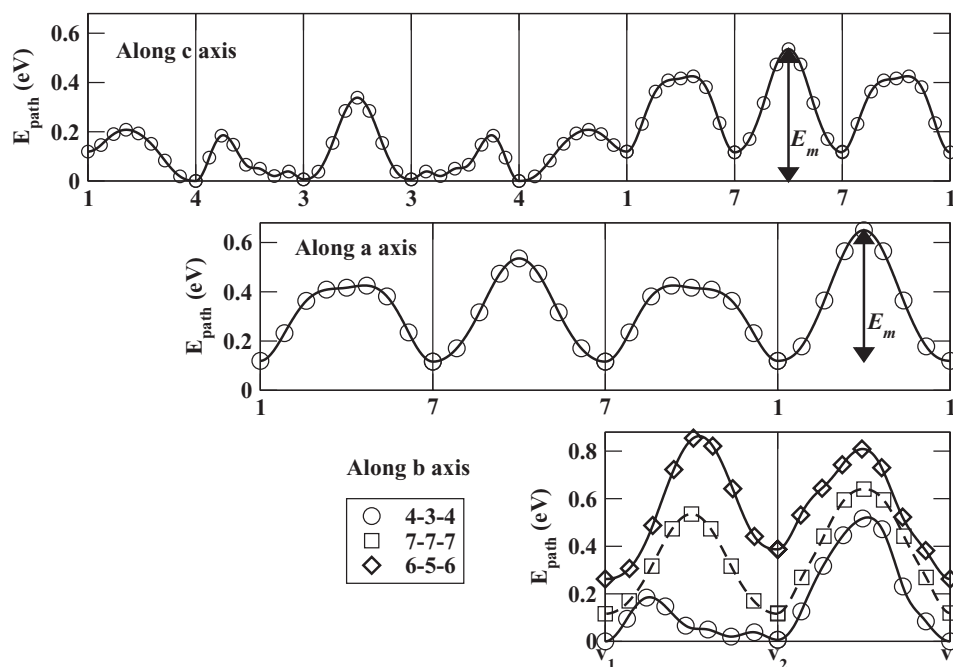**Figure 8.** Energy path diagrams for Li ion vacancy migration in $Li_7P_3O_{11}$ with net motion along the **c**, **a**, and **b** axes. For the **b**-axis plot the vacancy labels v_1 and v_2 are given in the legend. The energy scale is referenced to the lowest energy vacancy site **4**.
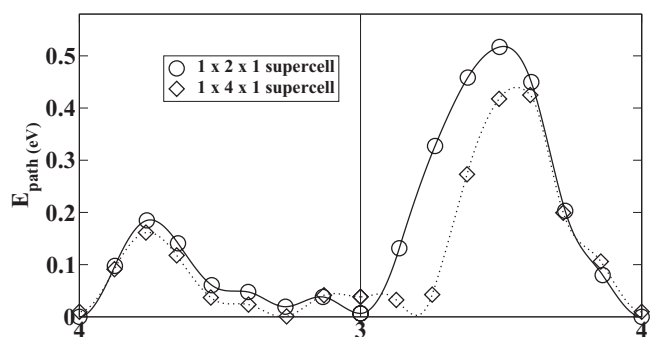

Figure 9. Energy path diagram for Li ion vacancy migration in $Li_7P_3O_{11}$ between vacancies sites **3** and **4** with net migration along the **b**-axis, comparing results from a $1 \times 2 \times 1$ supercell (as in Fig. 8) with that from a $1 \times 4 \times 1$ supercell. The vertical scale for the $1 \times 2 \times 1$ supercell calculation was fixed by choosing the energy of the **4** as the zero reference, while for the $1 \times 4 \times 1$ supercell the lowest energy along the interpolated path energy was set to 0.
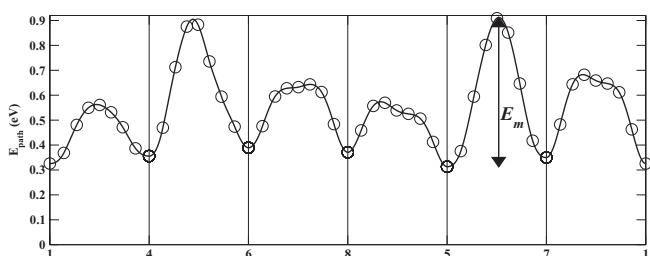

Figure 10. Energy path diagram for Li ion vacancy migration in $Li_8P_3O_{10}N$ between vacancies sites with a net migration path with components along all of the crystallographic axes. The energy scale is referenced to the lowest energy vacancy site **3**.

paths that avoid the **3** site are likely to have lower overall barriers. We observe that hops to sites near the N bonds are relatively favorable, but we find an overall barrier of $E_m = 0.60$ eV. The vacancy-interstitial formation is estimated to be $E_f = 1.2$ eV.

Discussion

The results presented for ionic conduction in $Li_7P_3S_{11}$ can be related to some of the attributes of superionic conductors[35] which typically have a number of partially occupied, low activation energy metastable sites. Applying this notion to $Li_7P_3S_{11}$, we have identified several extra metastable sites in the crystal structure which have approximately the same locations in the interstitial, vacancy, and combined vacancy-interstitial simulations. These sites can be occupied when excess Li is present or when a host Li is displaced to form a vacancy interstitial pair. In fact, Table X shows several examples of vacancy-interstitial combinations having very small formation energies E_f. The effects of these metastable sites can be seen trivially in the interstitial and combined simulations, but they are also important in the pure vacancy migration process. In this instance, the metastable low energy interstitial sites shown in Fig. 4 and listed in Table VIII affect the energy path profiles for the vacancy migration mechanisms shown in Fig. 2. The paths show a number of local energy minima due to the migrating lithiums passing near local potential minima caused by the metastable interstitial sites. For example, we have determined that the migrating host Li ion passes near the interstitial δ site in the vacancy process involving sites **1** and **2** along the **c**-axis and sites **2** and **7** along the **a**-axis. Similarly, the interstitial γ site is involved with the local energy minimum in the vacancy process involving the **3** and **4** sites along the **b**-axis and in the process involving the **7** and **4** sites along the **a**-axis which also involves the interstitial ε site. As a counter example to superionic behavior, the energy path analysis of Li ion vacancy diffusion in the $Li_7P_3O_{11}$ and $Li_8P_3O_{10}N$ materials indicate much less involvement of interstitial sites, a result which correlates with the relatively large vacancy-interstitial pair formation energies of $E_f \geq 0.5$ eV.

Another viewpoint for understanding Li ion migration in $Li_7P_3S_{11}$ is to identify general regions of the crystal which are energetically

unfavorable or favorable for Li ions. An example of the former is the region bounded by two P_2S_7 dimers in the local neighborhood of the inversion center and Li sites **5** and **6**. In this region, the metastable interstitial sites have relatively high energy, the metastable vacancy energies $E_v(\mathbf{5})$ and $E_v(\mathbf{6})$ are low (indicating that this region is less attractive to Li occupation), and the vacancy migration energies are high ($E_m \approx 0.4$ eV). The second type of region occurs between PS_4 monomer and P_2S_7 dimer components, especially in the neighborhood of the Li sites **3** and **4**. In this region, the metastable interstitial sites (β, γ, ϵ) have relatively low energy, the metastable vacancy site energies $E_v(\mathbf{3})$ and $E_v(\mathbf{4})$ are high (indicating that this region is more attractive to Li occupation), and the vacancy migration energies are low ($E_m \approx 0.2$ eV). These sets of properties suggest that Li ion migration in this material occurs primarily in the second region. This analysis is similar to that discussed by Onodera et al.[7] On the basis of geometry they identified a region of favorable Li ion diffusion which is similar to our second region.

Conclusions

We have modeled a stable structure for crystalline $Li_7P_3S_{11}$ with the $P\bar{1}$ space group and with approximate agreement with the experimental X-ray analysis[3] and neutron diffraction analysis.[7] Our formation energy results show the calculated structure to be stable with respect to decomposition into crystals of Li_3PS_4 and crystals of $Li_4P_2S_7$ crystals. Since crystals of $Li_4P_2S_7$ dimers have not been experimentally observed, it is more relevant that our results show that it is energetically favorable for $Li_7P_3S_{11}$ to decomposite into crystals of Li_3PS_4 monomers and crystals of $Li_4P_2S_6$ dimers plus excess S. This decomposition of $Li_7P_3S_{11}$ has been reported[5] under certain preparation conditions. The fact that high quality crystals of $Li_7P_3S_{11}$ have been prepared at room temperature by quenching techniques[1–7] indicates that there must be a high kinetic barrier which inhibits phase transformation at low temperature to the equilibrium structure.

Our analysis of likely Li ion migration processes find a low energy Li ion vacancy path with net motion along the crystallographic **b**-axis between the monomer and dimer groups having $E_m = 0.15$ eV. While we have attempted to make a systematic search for low energy migration paths through the crystal, we cannot claim to have examined all of the possible low energy paths. The vacancy-interstitial pair formation energy is estimated to be $E_f = 0.02 \pm 0.03$ eV. The results for E_m and E_f are in good agreement with the activation energy of $E_A = 0.12$ eV measured from temperature dependent conductivity experiments[2,4] and the activation of $E_A = 0.18$ eV found under different preparation conditions.[6] The small values of E_m and E_f found for this material are consistent with properties expected for a superionic conductor.

In addition, we have found a slightly less stable structure for this lithium thiophosphate material which we have labeled $Li_7P_3S_{11}^*$ with a total energy 0.07 eV per formula unit higher than the most stable structure. The computation of this metastable structure comes from optimizing the atomic coordinates determined in the neutron diffraction experiment[7] (instead of those determined in the X-ray diffraction experiment[3]). We have not found a transformation mechanism between the two structural forms. While the structural differences of the two structures are quite subtle, their effects on the Li ion migration properties was shown to be significant. For example, some of the Li ion vacancy sites are unstable (causing significant distortion of the host lattice) in the $Li_7P_3S_{11}^*$ structure while they are stable in the $Li_7P_3S_{11}$ structure. The interstitial Li sites also differ in the two structures. While more work is needed to relate the detailed computational results to experiment, the qualitative results indicate that subtle structural features of the electrolyte have the potential to significantly affect the Li ion migration.

It is also interesting to contrast the properties of lithium thiophosphates with the corresponding lithium phosphates and lithium phosphonitrides, both from the pure academic viewpoint and also from the technical viewpoint of possible insight into properties of LiPON electrolytes. We found that it is possible to simulate hypothetical crystals of both $Li_7P_3O_{11}$ and $Li_8P_3O_{10}N$ which have similar metastable

structures with the same $P\bar{1}$ space group. The minimum Li ion vacancy migration energies were found to be $E_m = 0.5$ and 0.6 eV for and the vacancy-interstitial pair formation energies were found to be $E_f = 0.8$ and 1.2 eV for $Li_7P_3O_{11}$ and $Li_8P_3O_{10}N$ respectively. While these structures have not been observed experimentally, the computed energies are comparable to results found in earlier studies on other crystalline materials related to LiPON electrolytes[36–38] and roughly consistent with measured migration energies on LiPON materials.[39] In the present study, the general results show that N does not obviously lower the migration barrier or reduce the vacancy-interstitial pair formation energy, but it does seem to increase the stability of the material in terms of decomposition into monomer and dimer fragments and in terms of ease finding the stable structure.

References

1. F. Mizuno, A. Hayashi, K. Tadanaga, and M. Tatsumisago, *Adv. Mater.*, **17**, 918 (2005).
2. F. Mizuno, A. Hayashi, K. Tadanaga, and M. Tatsumisago, *Solid State Ionics*, **177**, 2721 (2006).
3. H. Yamane, M. Shibata, Y. Shimane, T. Junke, Y. Seino, S. Adams, K. Minami, A. Hayashi, and M. Tatsumisago, *Solid State Ionics*, **178**, 1163 (2007).
4. M. Tatsumisago and A. Hayashi, *Journal of Non-Crystalline Solids*, **354**, 1411 (2008).
5. K. Minami, A. Hayashi, and M. Tatsumisago, *Journal of the Ceramic Society of Japan*, **118**, 305 (2010).
6. A. Hayashi, K. Minami, and M. Tasumisago, *J. Solid State Electrochem.*, **14**, 1761 (2010).
7. Y. Onodera, K. Mori, T. Otomo, A. C. Hannon, S. Kohara, K. Itoh, M. Sugiyama, and T. Fukunaga, *J. Phys. Soc. Jpn.*, **79**, 87 (2010), suppl. A; Proc. 3rd Int. Conf. Physics of Solid State Ionics (ICPSSI-3).
8. N. J. Dudney, *Interface*, **17**(3), 44 (2008).
9. N. A. W. Holzwarth, N. D. Lepley, and Y. A. Du, *Journal of Power Sources*, **196**, 6870 (2011), http://dx.doi.org/10.1016/j.jpowsour.2010.08.042.
10. P. Hohenberg and W. Kohn, *Physical Review*, **136**, B864 (1964).
11. W. Kohn and L. J. Sham, *Physical Review*, **140**, A1133 (1965).
12. D. Vanderbilt, *Phys. Rev. B*, **41**, 7892 (1990), USPP code is available from the website http://www.physics.rutgers.edu/˜dhv/uspp/.
13. P. Giannozzi, S. Baroni, N. Bonini, M. Calandra, R. Car, C. Cavazzoni, D. Ceresoli, G. L. Chiarotti, M. Cococcioni, I. Dabo, A. D. Corso, S. de Gironcoli, S. Fabris, G. Fratesi, R. Gebauer, U. Gerstmann, C. Gougoussis, A. Kokalj, M. Lazzeri, L. Martin-Samos, N. Marzari, F. Mauri, R. Mazzarello, S. Paolini, A. Pasquarello, L. Paulatto, C. Sbraccia, S. Scandolo, G. Sclauzero, A. P. Seitsonen, A. Smogunov, P. Umari, and R. M. Wentzcovitch, *J. Phys.: Condens. Matter*, **21**, 394402 (19pp) (2009), available from the website http://www.quantum-espresso.org.
14. J. P. Perdew and Y. Wang, *Phys. Rev. B*, **45**, 13244 (1992).
15. P. E. Blöchl, *Phys. Rev. B*, **50**, 17953 (1994).
16. N. A. W. Holzwarth, A. R. Tackett, and G. E. Matthews, *Computer Physics Communications*, **135**, 329 (2001), available from the website http://pwpaw.wfu.edu.
17. X. Gonze, B. Amadon, P. M. Anglade, J. M. Beuken, F. Bottin, P. Boulanger, F. Bruneval, D. Caliste, R. Caracas, M. Cote, T. Deutsch, L. Genovese, P. Ghosez, M. Giantomassi, S. Goedecker, D. R. Hamann, P. Hermet, F. Jollet, G. Jomard, S. Leroux, M. Mancini, S. Mazevet, M. J. T. Oliveira, G. Onida, Y. Pouillon, T. Rangel, G. M. Rignanese, D. Sangalli, R. Shaltaf, M. Torrent, M. J. Verstraete, G. Zerah, and J. W. Zwanziger, *Computer Physics Communications*, **180**, 2582 (2009), code is available at the website http://www.abinit.org.
18. N. D. Lepley and N. A. W. Holzwarth, *Transactions of the Electrochemical Society*, **35**(14), 39 (2011), http://dx.doi.org/10.1149/1.3644902.
19. OpenDX – The Open Source Software Project Based on IBM's Visualization Data Explorer – is available from the web site http://www.opendx.org.
20. A. Kokalj, *Journal of Molecular Graphics and Modelling*, **17**, 176 (1999).
21. Y. A. Du and N. A. W. Holzwarth, *Phys. Rev. B*, **81**, 184106 (15pp) (2010), http://link.aps.org/doi/10.1103/PhysRevB.81.184106.
22. H. J. Monkhorst and J. D. Pack, *Phys. Rev. B*, **13**, 5188 (1976).
23. H. Jónsson, G. Mills, and K. W. Jacobsen, in *Classical and Quantum Dynamics in Condensed Phase Simulations*, edited by B. J. Berne, G. Ciccotti, and D. F. Coker (World Scientific, Singapore, 1998) pp. 385–404.
24. G. Henkelman, B. P. Uberuaga, and H. Jónsson, *J. Chem. Phys.*, **113**, 9901 (2000).
25. G. Henkelman and H. Jónsson, *J. Chem. Phys.*, **113**, 9978 (2000).
26. D. R. Lide, ed., *CRC Handbook of Chemistry and Physics*, 90th Edition (CRC Press, Taylor & Francis Group, 2009) ISBN 13: 978-1-4200-9084-0.

27. T. Hahn, ed., *International Tables for Crystallography, Volume A: Space-group symmetry*, Fifth revised edition (Kluwer, 2002) ISBN 0-7923-6590-9. The symmetry labels used in this work are all based on this reference.

28. L. G. Cota and P. d. l. Mora, *Acta Cryst. B*, **61**, 133 (2005).

29. W. S. McDonald and D. W. J. Cruickshank, *Acta Cryst.*, **22**, 48 (1966).

30. A. G. Nord, *Acta Cryst. B*, **32**, 982 (1976).

31. K. Homma, M. Yonemura, T. Kobayashi, M. Nago, M. Hirayama, and R. Kanno, *Solid State Ionics*, **182**, 53 (2011).

32. R. Mercier, J.-P. Malugani, B. Fahyst, and G. Robert, *Acta Cryst.*, **B38**, 1887 (1982).

33. This notation differs from that presented in Ref. 18 with the mapping that sites 1,2,3,4,5,6,7 correspond to sites A, B, E, D, C, F, G, respectively.

34. G. Makov and M. C. Payne, *Phys. Rev. B*, **51**, 4014 (1995).

35. R. A. Huggins, *Advanced Batteries* (Springer, 2009) ISBN 978-0-387-76423-8.

36. Y. A. Du and N. A. W. Holzwarth, *Phys. Rev. B*, **78**, 174301 (2008).

37. Y. A. Du and N. A. W. Holzwarth, *Phys. Rev. B*, **76**, 174302/1 (2007).

38. Y. A. Du and N. A. W. Holzwarth, *Journal of the Electrochemical Society*, **154**, A999 (2007).

39. X. Yu, J. B. Bates, J. G. E. Jellison, and F. X. Hart, *Journal of the Electrochemical Society*, **144**, 524 (1997).